Catalysis Science & Technology

PAPER

View Article Online
View Journal | View Issue

Cite this: *Catal. Sci. Technol.*, 2014, 4, 3687

Surface stabilities and NO oxidation kinetics on hexagonal-phase $LaCoO_3$ facets: a first-principles study†

Xiao Liu,[ab] Zhengzheng Chen,[b] Yanwei Wen,[b] Rong Chen*[a] and Bin Shan*[bc]

Received 27th April 2014,
Accepted 13th June 2014

DOI: 10.1039/c4cy00538d

www.rsc.org/catalysis

$LaCoO_3$ perovskite has recently received great attention as a potential alternative to precious metal based NO oxidation catalysts. We report here a comprehensive first-principles study of the NO oxidation kinetics on differently re-constructed hexagonal-phase $LaCoO_3$ facets. Among the 42 low-index facets considered, the $(1\bar{1}02)$ LaO-, $(\bar{1}104)$ O_2- and (0001) LaO_3-terminated facets were found to be thermodynamically stable and likely to be exposed in $LaCoO_3$ oxide nanoparticles. Among these stable facets, the (0001) LaO_3-terminated surface is catalytically most active towards NO oxidation, with the reaction proceeding through the mono-vacancy Mars–van Krevelen mechanism. Our study shed light on the atomistic scale NO oxidation mechanism on $LaCoO_3$ facets and can aid further optimization of the catalyst.

1. Introduction

Diesel engines have aroused great interest in recent years due to their high fuel efficiencies and low green-house gas emissions.[1] However, the lean burn exhaust, which contains considerable amounts of nitrogen oxides (NO_x), poses a great threat to human health and the environment. Two mainstream technologies are being utilized by auto manufacturers to remove the hazardous NO_x emissions. The first strategy is called selective catalytic reduction (SCR), which involves the partial oxidation of NO to NO_2 through diesel engine oxidation (DOC) catalysts and subsequent reactions with ammonia to form environmentally benign N_2. The other popular strategy is using a lean NO_x trap (LNT), which utilizes the NO_2 storage and release mechanism of LNT trapping materials such as $Pt/BaO/Al_2O_3$ for NO_x reduction. In both cases, a higher concentration of NO_2 in the exhaust stream proves to be beneficial for the catalytic process,[2] driving a considerable interest in the scientific community in search of catalysts for efficiently oxidizing NO into NO_2. Traditionally, platinum (Pt) metal is the major material component in automobile catalytic convertors for NO oxidation due to its durability against oxidation and high catalytic activity, originating from its unique d-orbital electronic structure.[3,4] However, with the urge for stricter NO_x control in the next-generation emission standards, its practical development and large-scale applications are hindered by limited reserves and supply. Pt's rising price and the higher catalyst loading required for the stricter emission standards also likely raise cost concerns for auto manufacturers. To reduce the overall catalyst cost, precious metal catalysts need to be replaced by new earth-abundant, cost effective, and high performance catalysts.

A significant amount of work has been undertaken in the field of emission control technology to search for alternative NO oxidation catalysts. Rare-earth and transition metal oxide catalysts have long been considered as some of the most promising candidates for substituting expensive precious metal components, as they show not only thermal stability towards sintering and oxidation, but also excellent catalytic activity for many important chemical reactions, such as CO oxidation, hydrocarbon oxidation, NO oxidation, NO_x storage and reduction.[5–10] Li *et al.*[11] have synthesized $Mn–Ce–O_x$ catalysts at various ratios *via* co-precipitation, low temperature solid phase reaction and citric acid methods and studied the activity for NO oxidation. While MnO_x has shown promising catalytic activity, it suffers from aging loss of catalytic activity during an extended period of catalytic reactions. More recently, Wang *et al.* have reported a mullite based oxide catalyst where a Mn–Mn dimer serves as the catalytic

[a] *State Key Laboratory of Digital Manufacturing Equipment and Technology and School of Mechanical Science and Engineering, Huazhong University of Science and Technology, Wuhan 430074, Hubei, People's Republic of China. E-mail: rongchen@mail.hust.edu.cn*
[b] *State Key Laboratory of Material Processing and Die and Mould Technology and School of Materials Science and Engineering, Huazhong University of Science and Technology, Wuhan 430074, Hubei, People's Republic of China. E-mail: bshan@mail.hust.edu.cn*
[c] *Department of Materials Science and Engineering, The University of Texas at Dallas, Richardson, Texas 75080, USA*

† Electronic supplementary information (ESI) available: Description of detailed structural information on hexagonal $LaCoO_3$. See DOI: 10.1039/c4cy00538d

reaction center for NO oxidation.[12] Among the different types of oxides investigated thus far, perovskite structures (ABO_3, with A = a rare-earth cation and B = a transition metal cation), particularly $LaCoO_3$, have attracted much attention as Pt replacement catalysts. Wen *et al.* and Zhou *et al.* have studied the NO oxidation activity of cerium (Ce) and copper (Cu) doped $LaCoO_3$ perovskite and showed that A and B site substitution can greatly enhance the performance.[13,14] Kim *et al.*[15] found that strontium (Sr) doped $LaCoO_3$ has great performance for NO oxidation, which is comparable with commercial Pt/γ-Al_2O_3 based catalysts. On the theoretical side, efforts in understanding the electronic structures of $LaCoO_3$ materials as well as its surface stabilities are also emerging. Kahn *et al.* have studied the stability of cubic $LaCoO_3$ using a Born shell empirical model and predicted the Co-terminated (111) surface and LaCoO-terminated (110) surface to be the most stable.[16] On the other hand, to take into account the charge redistribution in a self-consistent manner and improve the accuracy of stable facet prediction, Chen *et al.* have used *ab initio* thermodynamics models to construct the crystal morphology of cubic $LaCoO_3$ nanoparticles and they found that the LaO-terminated (001) surface is more stable.[17] However, both stability studies focused mostly on the structural and electronic properties of cubic phase $LaCoO_3$, which is not in agreement with the experimental characterizations of the $LaCoO_3$ ground state. A number of studies have revealed that hexagonal phase $LaCoO_3$ is lower in energy than cubic phase $LaCoO_3$,[18,19] in good agreement with the XRD identification of the $R\bar{3}c$ space group of the $LaCoO_3$.[20,21] Recently, Choi *et al.* have studied the NO oxidation reaction on cubic-phase $LaCoO_3$ with Jahn–Teller (J–T) distortion and discussed the role of Sr in enhancing the oxygen exchange ability on one particular facet.[22] To our best knowledge, a detailed and comprehensive knowledge of NO oxidation kinetics on different $LaCoO_3$ perovskite facets is still lacking. To further optimize the nanoparticle catalyst for industrial use, it is of great importance to gain a deep understanding of the underlying active sites and reaction mechanisms at the atomic level.

In this study, we report comprehensive first-principles calculations on the surface stabilities of differently re-constructed hexagonal-phase $LaCoO_3$ oxide catalysts and the NO oxidation kinetics on stable facets. By comparing surface grand potentials, we identified the stable facets of $LaCoO_3$ in different chemical environments. Wulff-construction was used as a first-order approximation to predict the exposed facets in $LaCoO_3$ nanoparticles. NO oxidation energetics and kinetics on these catalytically active facets were investigated in detail. Our results show that the LaO_3-terminated surface is the catalytically most active surface for NO oxidation, whose surface area depends sensitively on the cobalt chemical potential. The rest of the paper is organized as follows: in section II, we briefly summarize the model system and computational methodology. Detailed results and discussions are presented in section III. Finally, a summary and conclusions are given in section IV.

2. Computational models and methods

For comparison purposes, the atomic structure of cubic phase $LaCoO_3$ is shown in Fig. 1(a), with La atoms (green spheres) in eight corners, one Co atom (blue sphere) at the center of the unit cell, and O atoms (red spheres) located at the center of the facets. Fig. 1(b) shows the cross section of the cubic (100)-CoO_2 surface. A distinctive feature of the cubic phase is the Co–O–Co bond angle of 180°. The hexagonal phase $LaCoO_3$ also consists of octahedral CoO_6 with La atoms in the vertex, as shown by the red dotted lines in Fig. 1(c). However, the structure and symmetry are different from the cubic phase due to the J–T distortion, which causes the distortions in the red dotted framework, making it no longer the unit cell of the structure.[23,24] Fig. 1(d) shows the $(1\bar{1}02)$-CoO_2 surface in the hexagonal phase, which roughly corresponds to the (100)-CoO_2 surface in the cubic phase. Note that the Co–O–Co bond angle in the hexagonal phase is 161.9° instead of 180°. J–T distortion also makes certain symmetric directions in the cubic phase inequivalent. For example, the eight equivalent <111> directions in the cubic phase now split into two <0001> and six $<\bar{1}101>$ directions in the hexagonal phase. The twelve <110> directions in the cubic phase now become six $<11\bar{2}0>$ and six $<\bar{1}104>$ directions in the hexagonal phase (the detailed correspondence relationships can be found in the ESI†). In the surface stability discussion part, we have considered all these non-equivalent directions.

All calculations were performed within the density functional theory (DFT)[25,26] framework using the plane wave basis as implemented in the Vienna *ab initio* simulation package (VASP).[27–29] The exchange and correlation energies were

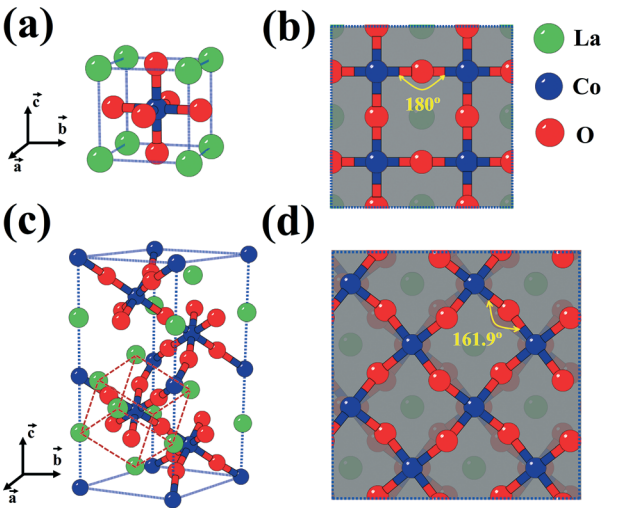

Fig. 1 Atomic structures of (a) cubic phase and (c) hexagonal phase $LaCoO_3$. The similar cubic structure, which is not the unit cell of the hexagonal phase, has been labeled with red dotted lines. Top view of (b) the (100)-CoO_2 surface in the cubic phase and (d) the $(1\bar{1}02)$-CoO_2 surface in the hexagonal phase have been presented.

treated by the generalized gradient approximation (GGA) with the Perdew–Burke–Ernzerhof (PBE)[30] form generated by the projector augmented wave (PAW)[31] method, as such a functional was shown to give reasonable results for molecular adsorption energies.[32,33] For Co ions, the outer electrons ($3d^8 4s^1$) were treated as valence electrons and the core electrons were replaced by effective potentials. While standard DFT methods have been successfully used to investigate the electronic structures and catalytic properties of metal and metal oxide surfaces, they fail to obtain the correct electronic structure for strongly correlated systems such as transition metal oxides and rare-earth compounds. To overcome the inaccuracy of standard DFT in describing the partially filled d-states in Co^{3+} ions, we used GGA + U formalism to correct the on-site Coulomb and exchange interactions for localized d orbitals.[34] Several methods have been proposed to determine the magnitude of the onsite Hubbard-type U and detailed procedures in getting U values have been discussed extensively in the review paper by Lee *et al.*[23] In general, the inclusion of U correction is shown to yield much better results in terms of describing electronic structures and can recover most of the bulk and surface properties, as illustrated in the case of predicting CO/NiO and NO/NiO adsorption energies.[35,36] Recently, Ma *et al.* performed a systematic comparative study on the influence of U, J parameters in describing $LaCoO_3$ perovskite properties and found a set of optimal values of U = 3.40 eV and J = 0.49 eV that offer results in good agreement with experiments.[37] We adopted the aforementioned U, J parameters in the present work. Recent progresses in GW calculations[38,39] and hybrid functional calculations[40,41] can in principle yield reliable results with less empirical parameters. However, due to the high computational demand of these methods and the practical need of using a large unit cell for modelling surface reactions, we chose GGA + U formalism as a good compromise between accuracy and computational efficiency.

In both bulk and surface calculations, the geometry optimization is performed until the Hellmann–Feynman force on each atom is smaller than 0.05 eV $Å^{-1}$. An energy cutoff of 400 eV is employed on the plane wave basis. The numerical integration in the first Brillouin zone is performed using a Monkhorst–Pack[42] grid of 7 × 7 × 3 for the bulk, and 3 × 3 × 1 for the surface, respectively. To check the convergence, we have compared the total energy to the ones calculated with finer k-mesh. The difference is smaller than 5 meV. The $LaCoO_3$ surfaces were represented by periodic slabs consisting of at least 11 layers. A vacuum with thickness of 15 Å is adopted to avoid interactions between slabs. In order to discuss the thermodynamic stabilities of the surfaces, we have calculated the surface grand potential (Ω), which has been previously used in studies of low-index surfaces of binary and ternary compounds.[43,44] By assuming that the slab is always in equilibrium with the bulk $LaCoO_3$, we have the following constraint:

$$E_{LaCoO_3} = \mu_{LaCoO_3} = \mu_{La} + \mu_{Co} + 3\mu_O \quad (1)$$

where E_{LaCoO_3} is the total energy of the bulk per $LaCoO_3$ formula unit and μ_i is the chemical potential of the i-th species. By substituting μ_{La}, Ω can be expressed as a function of μ_O and μ_{Co}:

$$\Omega = \frac{1}{2S}\left[E_{slab} - N_{La}E_{LaCoO_3} - \mu_O\left(N_O - 3N_{La}\right) - \mu_{Co}\left(N_{Co} - N_{La}\right)\right] \quad (2)$$

where E_{slab} is the energy of the slab, N_{La}, N_{Co} and N_O are the number of atoms in the slab, S is the surface area of the slab and the factor of 1/2 comes from the fact that the slab has identical top and bottom terminations. Boundary conditions have also been considered to define the accessible region of the thermodynamic system. To avoid condensation of elemental La, Co or O_2(g) on the surfaces, the following three constraints have to be satisfied:

$$\mu_{Co} + 3\mu_O \geq E_{LaCoO_3} - \mu_{La} \quad (3)$$

$$\mu_{Co} \leq \mu_{Co}^0 \quad (4)$$

$$\mu_O \leq \mu_O^0 \quad (5)$$

where μ_{La}^0 (μ_{Co}^0) is the cohesive energy of La (Co) bulk atoms, and μ_O^0 is $E_{O_2}/2$, where E_{O_2} is the energy of an O_2 molecule. Detailed derivation of the boundary conditions can be found in ref. 43.

After obtaining Ω for all ideal and re-constructed surfaces, we employed Wulff-construction[45] as a first-order approximation to predict the exposed facets of $LaCoO_3$ perovskite nanoparticles. The distances between the parallel exposed facets are proportional to Ω, which determines the shape of the nanoparticles. The followed nanoparticles are all generated using Visualization for Electronic and Structural Analysis (VESTA) software.[46] Two quantities are of great importance to the activity of exposed oxide surfaces: the oxygen vacancy energy (E_{Ov}) and the highest energy barrier (ΔE_{TS}) in the minimum energy path (MEP) of the NO oxidation process. In the current work, E_{Ov} is calculated using the following formula:

$$E_{Ov} = E_{sys\text{-}O} - E_{sys} + E_{O_2}/2 \quad (6)$$

where, E_{sys} and $E_{sys\text{-}O}$ are the total energies of ideal and defective (with one oxygen vacancy) hexagonal $LaCoO_3$ slabs, respectively. For the MEP of NO oxidation, the climbing image nudged elastic band method (CI-NEB)[47] was employed. Initial approximations to reaction paths are obtained by linear interpolation between the reactant and product configurations. Six intermediate images were used for all the CI-NEB calculations, which map the MEP with reasonable accuracy. Moreover, a frequency calculation has been performed to check the transition states and only one imaginary frequency exists for each transition state.

3. Results and discussion

3.1. Bulk properties

The calculated bulk properties of $LaCoO_3$ in the hexagonal phase, such as the lattice constants (a and c), band gap (E_g), magnetic moment (μ) and total energy (E_{LaCoO_3}), are tabulated in Table 1. During the optimization of lattice constants, we keep $\alpha = \beta = 90°$, $\gamma = 120°$ and $a = b$. The values of a and c are optimized to get the minimal total energy. Experimental values are also listed for comparison. The results show that the hexagonal phase of $LaCoO_3$ is indeed the ground state, since the total energy per unit is about 0.2–0.3 eV lower than that of the cubic phase. Note that the non-spin-polarized model (NSP) with PBE + U yields almost identical results with the spin-polarized model (SP) and it recovers the experimental lattice constant within 0.3%,[48] and the band gap within 0.01 eV.[49] Previous theoretical and experimental studies also indicate that $LaCoO_3$ is a nonmagnetic semiconductor with Co^{3+} in the low-spin state ($S = 0$, $t_{2g}^6e_g^0$).[50–52] Overall, the NSP model is computationally efficient and yields reliable results about the structural and electronic properties of $LaCoO_3$. It is thus employed in all the following calculations. For gas molecules such as O_2, NO and NO_2, their total energies have been corrected by spin polarizations using the same techniques as reported in previous studies.[53–55]

The calculated band structure and density of states (DOS) are shown in Fig. 2. The sharp anti-bonding peak at around 4.5 eV above the Fermi level represents the vacant La 4f orbitals. The occupied 3d orbitals of Co were split into t_{2g} (−5–3.5 eV) and e_g (−1–0 eV) *via* the cubic symmetry breaking process. It is found the Co-3d and O-2p orbitals contribute most to the valence band maximum and the conduction band minimum. Fig. 2 also shows strong hybridization between Co-3d and O-2p orbitals, indicating the stability of CoO_6 octahedrons in $LaCoO_3$.

3.2. Surface stability

According to the symmetry of hexagonal phase $LaCoO_3$, we have considered six low-index crystalline plane families: {1$\bar{1}$02}, {0001}, {$\bar{1}$101}, {11$\bar{2}$0}, {$\bar{1}$104}, and {10$\bar{1}$0}. Each family has two different terminations. We label them in the format

Table 1 Lattice constants a ($a = b$) and c, band gap (E_g), magnetic moment (μ) and total energy (E_{LaCoO_3}) per unit of $LaCoO_3$. The values in the parentheses in the last column are for the cubic phase. For PBE and PBE + U (U = 3.40 eV), we have considered both spin-polarized (SP) and non-spin-polarized (NSP) models. For comparison, the available experimental data are listed in the bottom row as well

	a (Å)	c (Å)	E_g (eV)	μ (μ_B)	E_{LaCoO_3} (eV)
SP	5.426	12.991	0.00	0.02	−38.00 (−37.72)
NSP	5.427	12.949	0.00	—	−37.99 (−37.74)
SP-U	5.426	12.991	0.63	0.00	−36.15 (−35.90)
NSP-U	5.424	12.960	0.61	—	−36.14 (−35.90)
Exp.	5.426[a]	12.991[a]	0.60[b]	0.00	—

[a] Ref. 48. [b] Ref. 49.

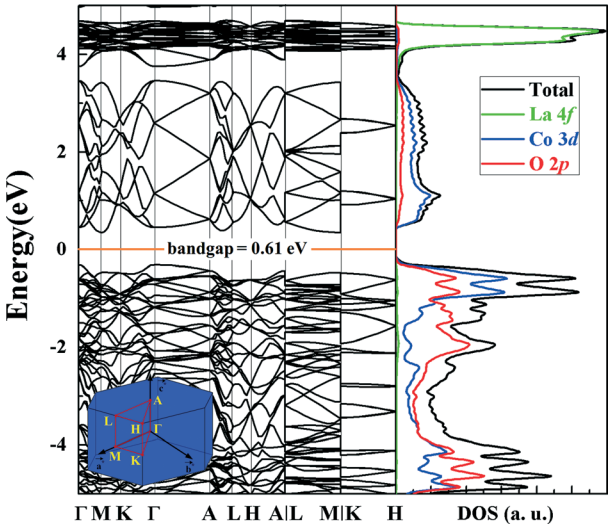

Fig. 2 The band structure and DOS of $LaCoO_3$. The total density of states (DOS) and partial DOS (PDOS) of La 4f, Co 3d and O 2p orbitals are plotted with black, green, blue and red lines, respectively.

(orientation)-terminated element, such as the (1$\bar{1}$02)-LaO and -CoO_2, (0001)-LaO_3 and -Co, ($\bar{1}$101)-LaO_3 and -Co, (11$\bar{2}$0)-LaCoO and -O_2, ($\bar{1}$104)-LaCoO and -O_2, (10$\bar{1}$0)-LaCoO and -O_2 facets, and present their detailed structures in Fig. S2–S5 in the ESI.† Since these facets have the nominal charges of La (+3e), Co (+3e) and O (−2e) atoms, they are polarized and may undergo reconstruction.[56] We used $p(1 \times 1)$ to represent an ideal surface, and $p(2 \times 1)$ and $p(2 \times 2)$ to represent two different kinds of reconstructions. Moreover, for the O_2 terminated surfaces (10$\bar{1}$0)-O_2, (11$\bar{2}$0)-O_2 and ($\bar{1}$104)-O_2, $c(2 \times 1)$ and $c(2 \times 2)$ reconstructions were also considered.[57] All the reconstruction rules considered are presented in Fig. S6 in the ESI.†

The surface grand potentials (Ωs) of a total of 42 facets have been calculated. The grand surface energy at $\Delta\mu_{Co} = \Delta\mu_O = 0$ eV (Ω_0) and the stoichiometric ratio of the slabs, where $\Delta\mu_{Co} = \mu_{Co} - \mu_{Co}^0$ and $\Delta\mu_O = \mu_O - \mu_O^0$, are summarized in Table S1 in the ESI.† By choosing the surface with the lowest Ω at each point in the accessible region (defined by the confinements given in eqn (3)–(5)), the surface stability diagram of hexagonal phase $LaCoO_3$ can be constructed as shown in Fig. 3(a). We find that three terminations out of the 42 facets are thermodynamically most favorable: ($\bar{1}$104)-O_2 $c(2 \times 2)$, (0001)-LaO_3 $p(1 \times 1)$ and (1$\bar{1}$02)-LaO $p(1 \times 1)$, whose surface configurations are shown in Fig. 3(b)–(d), respectively. Compared to the cubic phase, the O_2 terminated surface is stable under appropriate chemical potential regions, in addition to the LaO_3- and LaO-terminated surfaces that were predicted to exist in the cubic phase.[17] This may be related to the J–T distortion between the hexagonal and cubic phases, which affects the oxygen binding on the surface. The (1$\bar{1}$02)-LaO $p(1 \times 1)$ surface (Fig. 3(d)) covers the greatest part of the diagram. This may be attributed to the fact that the (1$\bar{1}$02)-LaO $p(1 \times 1)$ surface does not require the cleaving of stable CoO_6 octahedrons, which keeps the system in a

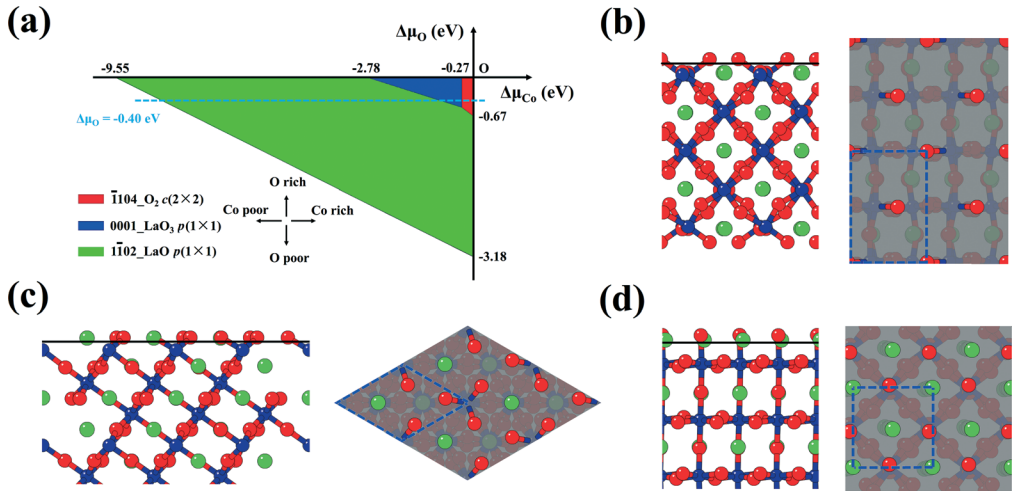

Fig. 3 (a) The stability graph of the low-index surfaces of hexagonal $LaCoO_3$. The actual most stable termination is represented as a function of the excess O and Co chemical potentials $\Delta\mu_O$ ($\Delta\mu_O = \mu_O - \mu_O^0$, vertical) and $\Delta\mu_{Co}$ ($\Delta\mu_{Co} = \mu_{Co} - \mu_{Co}^0$, horizontal). The side and top views of the (b) ($\bar{1}104$)-O_2 $c(2 \times 2)$, (c) (0001)-LaO_3 $p(1 \times 1)$ and (d) ($1\bar{1}02$)-LaO p(1 × 1) surfaces in (a).

relatively stable structure. As shown in Fig. 3(d), both La and O atoms on the surface are located in their crystalline lattice positions, except for small out-of-surface displacements. The other two terminations, ($\bar{1}104$)-O_2 $c(2 \times 2)$ and (0001)-LaO_3 $p(1 \times 1)$, would become the most stable surfaces only in O- and Co-rich environments, respectively. Under realistic experimental conditions, the range of accessible oxygen chemical potential would generally be within the range of −0.2 to −0.6 eV.[58] We therefore chose $\Delta\mu_O$ = −0.40 eV (marked as the dotted line in Fig. 3a) as a representative case and plotted the grand potential Ωs of the different facets with Co increasing from −8.35 to 0 eV in Fig. 4(a). Shifting to other oxygen chemical potentials within the accessible range would only yield minor numerical corrections without changing the overall picture of the reaction mechanism. When $\Delta\mu_{Co}$ is very negative, ($1\bar{1}02$)-LaO $p(1 \times 1)$ is most stable. By increasing $\Delta\mu_{Co}$ along the dotted line, the concentration of La atoms decreases in the environment. Consequently, surfaces with lower La coverage (θ_{La}) become more stable. When $\Delta\mu_{Co} >$ −0.88 eV, the (0001)-LaO_3 $p(1 \times 1)$ surface with θ_{La} = 0.25

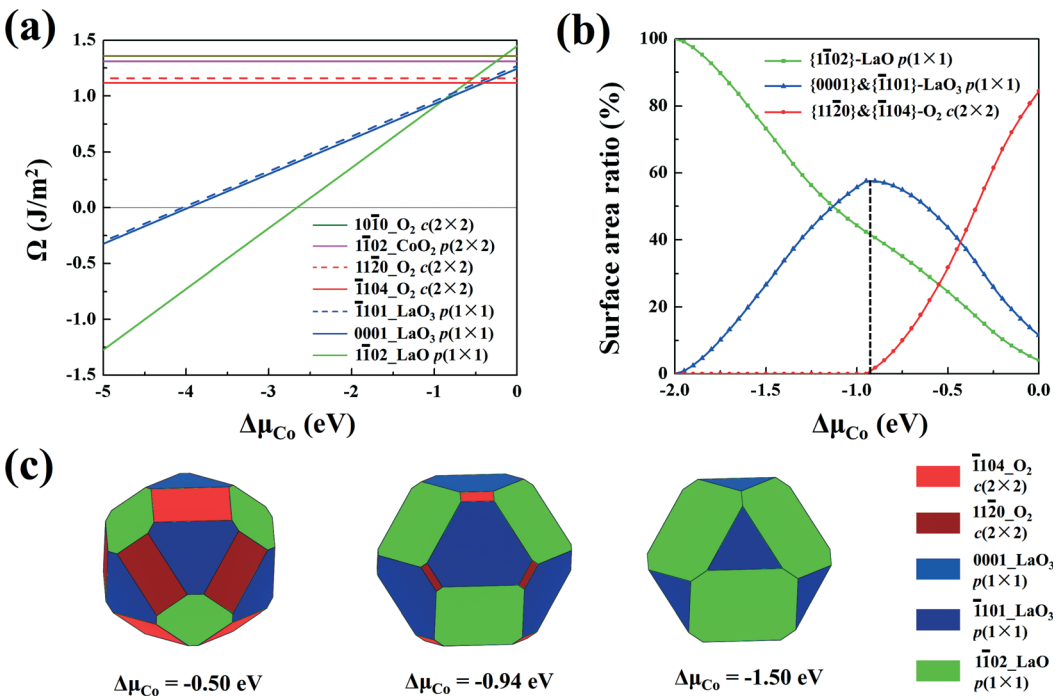

Fig. 4 (a) Stability diagram of different terminations of $LaCoO_3$ with $\Delta\mu_O$ = −0.40 eV. (b) The relationship between the area of the exposed surfaces of the NPs and $\Delta\mu_{Co}$. (c) The nanoparticles by Wulff-construction with different $\Delta\mu_{Co}$.

becomes the most stable facet. Further, when $\Delta\mu_{Co}$ increases to −0.27 eV, corresponding to extremely La-poor conditions, the ground stable facet turns to the $(\bar{1}104)$-O_2 $c(2 \times 2)$ termination, on which $\theta_{La} = 0$. Interestingly, in the whole accessible region, none of the most stable surfaces contain directly exposed Co atoms. One possible explanation is that the dangling 3d–e_g orbitals of Co atoms are energetically unfavorable when exposed on surfaces.

3.3. Nanoparticles and exposed facets

Based on the calculated Ω, we have constructed $LaCoO_3$ nanoparticles (NPs) at different $\Delta\mu_{Co}$ with $\Delta\mu_O \equiv -0.40$ eV using the Wulff-construction method. It should be noted that Wulff-constructions only apply to bulk particles in a strict sense. However, given the relatively large diameter of oxide nanoparticles, the Wulff-construction should serve as a good first-order approximation.[59] We present quantitatively in Fig. 4(b) the area of the exposed surfaces of the NPs as a function of $\Delta\mu_{Co}$. The area of $\{\bar{1}104\}$-O_2 and $\{1\bar{1}02\}$-O_2 are sensitive to $\Delta\mu_{Co}$; they cover 84% of the total area when $\Delta\mu_{Co}$ = 0 eV, but completely disappear when $\Delta\mu_{Co}$ decreases to −0.96 eV. On the other hand, $\{\bar{1}101\}$-LaO_3 facets become dominant with -1.12 eV $< \Delta\mu_{Co} <$ −0.43 eV. When $\Delta\mu_{Co}$ is −0.94 eV, its coverage reaches the maximum (58%). When $\Delta\mu_{Co}$ is lower than −2.00 eV, $\{1\bar{1}02\}$-LaO is the only exposed surface. Due to the complicated dependence of exposed surfaces on the environment, it is necessary to examine the catalytic activity of each surface in order to predict the best working conditions of $LaCoO_3$ NPs.

We present three representative shapes of generated NPs in three specific $\Delta\mu_{Co}$ conditions, ranging from Co poor to Co rich, in Fig. 4(c). When $\Delta\mu_{Co} = -0.50$ eV, the profile of a NP has twenty-six facets, consisting of 6 $\{\bar{1}104\}$-O_2, 6 $\{11\bar{2}0\}$-O_2, 2 $\{0001\}$-LaO_3, 6 $\{\bar{1}101\}$-LaO_3 and 6 $\{1\bar{1}02\}$-LaO facets, respectively. As shown in Fig. 4(a), the Ω of $(\bar{1}101)$-LaO_3 $p(1 \times 1)$ is parallel to and only slightly higher than that of (0001)-LaO_3 $p(1 \times 1)$, because their structures are similar except for the slight displacement of oxygen atoms. Thus, although only three facets appear in the stability diagram of Fig. 3(c), $(\bar{1}101)$-LaO_3 and $(11\bar{2}0)$-O_2 may also be exposed on the surface and participate in the catalytic reaction. $(11\bar{2}0)$-O_2 and $(\bar{1}104)$-O_2 have the same tendency. By changing the value of $\Delta\mu_{Co}$, the relative area of the exposed terminations will vary accordingly. The area of $\{\bar{1}104\}$-O_2 and $\{1\bar{1}02\}$-O_2 decreases considerably when $\Delta\mu_{Co}$ decreases from −0.50 eV to −0.94 eV. Moreover, when $\Delta\mu_{Co} < -1.50$ eV, the Ω of the $(1\bar{1}02)$-LaO termination is much lower than that of others. The NPs therefore tend to exhibit a cubic shape wrapped by 6 $\{1\bar{1}02\}$-LaO facets.

3.4. NO oxidation kinetics

NO oxidation processes on the $LaCoO_3$ facets are primarily *via* the Mars–van Krevelen (M–vK) mechanism,[60] which is also the dominant mechanism in many other oxidation processes on metal oxides surfaces.[61,62] Moreover, the results of temperature programmed desorption and isotopic exchange (TPIE) experiments by Choi *et al.* also indicate that surface species and oxygen exchange processes correlate with NO oxidation activity, which is also consistent with the M–vK mechanism.[22] For NO oxidation, the M–vK mechanism consists of two typical steps: 1) a NO molecule reacts with one lattice O atom and forms NO_2, and 2) an O_2 molecule occupies the created oxygen vacancy from the previous step, creating an active adsorbed O* species, which reacts with another NO molecule. This scenario can be regarded as a mono-vacancy (Mv) M–vK mechanism, as shown in Scheme 1. We have also considered a di-vacancy (Dv) M–vK mechanism in which two NO molecules react with two O atoms from lattice sites sequentially, and two vacancies are subsequently filled *via* the dissociation of O_2, completing a full catalytic cycle, as shown in Scheme 2.

We first calculated the E_{Ov} of the possible exposed surfaces and listed the results in Table 2. The $(1\bar{1}02)$-LaO $p(1 \times 1)$ surface has the highest E_{Ov} (4.18 eV), which suggests that this surface is not active since O atoms bind too strong to the lattice sites and it is difficult for them to escape. The other two re-constructed surfaces, $(\bar{1}104)$-O_2 $c(2 \times 2)$ and $(11\bar{2}0)$-O_2 $c(2 \times 2)$, exhibit somewhat lower but still considerably high E_{Ov} at 2.29 eV and 2.74 eV, respectively. Since the reconstructed surfaces intrinsically have a considerable number of isolated O vacancies (Fig. 3b) that may play a role in the oxidation process, these two surfaces are included in our following discussions. On the other hand, the E_{Ov} of the (0001)-LaO_3 $p(1 \times 1)$ and $(\bar{1}101)$-LaO_3 $p(1 \times 1)$ surfaces are close to zero,

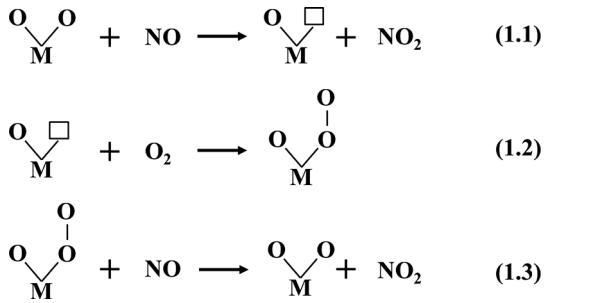

Scheme 1 The sequence of elementary steps for NO oxidation on an oxide surface based on a Mv M–vK mechanism.

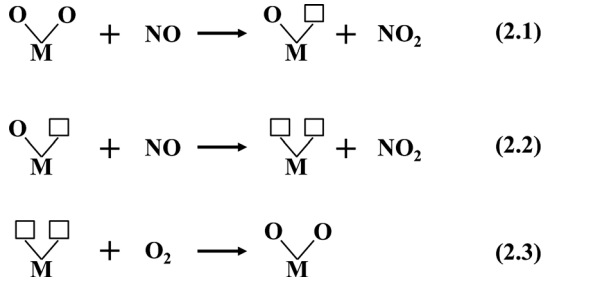

Scheme 2 The sequence of elementary steps for NO oxidation on an oxide surface based on a Dv M–vK mechanism.

Table 2 The oxygen vacancy formation energy (E_{Ov}) of possible exposed surfaces by Wulff-construction

Surfaces	$(1\bar{1}02)$-LaO $p(1 \times 1)$	(0001)-LaO_3 $p(1 \times 1)$	$(\bar{1}101)$-LaO_3 $p(1 \times 1)$	$(\bar{1}104)$-O_2 $c(2 \times 2)$	$(11\bar{2}0)$-O_2 $p(2 \times 2)$
E_{Ov} (eV)	4.38	0.09	0.19	2.29	2.74

indicating the high activity of O atoms and the relative easiness of oxygen vacancy formation on these facets. Thus in addition to reaction routes on an ideal surface, NO oxidation on these facets with oxygen vacancies present was also taken into account.

The MEP of NO oxidation on the $(\bar{1}104)$-O_2 $c(2 \times 2)$ re-constructed surface is first discussed and presented in Fig. 5, in which each stage means a stable state of reactant or product along the reaction path. Due to the high energy cost of removing the second lattice oxygen with an E_{Ov} larger than 2 eV, vacancy pairing is a rare event and the Mv M–vK mechanism is generally the preferred reaction route on the re-constructed surface.[33] According to the Mv M–vK mechanism in Scheme 1, the reaction will initiate at (1.2) as an O_2 molecule will occupy the lattice vacancy and form O_2* (stage 2). Then a NO molecule binds with the protruding O atom and forms an NO_2 molecule adsorbed to the surface (stage 3 to stage 4). The energy barrier for the detachment of the NO_2 molecule (ΔE_{stage4}) is 0.56 eV. The second half of the MEP includes the formation of Co-nitrite ($-NO_2$) species on the surface, resulting from the binding of the second NO molecule and one O atom in the lattice sites (stage 6 to stage 7). Among all the reaction paths, NO_2 desorption is the rate-determining step (RDS) since the corresponding barrier (ΔE_{stage7}, 1.26 eV) is the highest along the MEP. The whole reaction can be summarized as $2NO + O_2 \rightarrow 2NO_2$ with 2.31 eV exothermically. In addition, we have calculated the MEP of NO oxidation on the $(11\bar{2}0)$-O_2 $c(2 \times 2)$ surface and the results are presented in Fig. S7.† We notice the RDS is also the desorption of the NO_2 molecule with an energy barrier of 1.18 eV, similar to the case of the $(\bar{1}104)$-O_2 $c(2 \times 2)$ surface. This suggests that the slight structural variation among the different surface orientations within the same group will not affect the catalytic process.

For the (0001)-LaO_3 $p(1 \times 1)$ facets, since the oxygen vacancy formation is small, it is expected that ideal facets and defective facets with oxygen vacancies are likely to co-exist under realistic experimental conditions. Consequently, we have studied the MEP of NO oxidation in both cases. The MEP on an ideal (0001)-LaO_3 surface also follows the Mv M–vK mechanism (Scheme 1), as shown in Fig. 6, in which the transition states are labelled as TS. The oxidation reaction initiates with NO (g) adsorbing onto the O site to form Co-nitrite ($-NO_2$). The adsorbed NO then binds with one O atom from a lattice site and desorbs from the surface as a NO_2 molecule. Interestingly, we find that the desorption process is divided into two steps due to the attraction of neighboring La atoms to the NO_2 molecule, which is consistent with previous experimental results.[63] Firstly, the NO_2 molecule overcomes an energy barrier of 0.78 eV to desorb from the surface with an oxygen vacancy left behind (stage 2 to stage 3). However, the desorbed NO_2 molecule is still

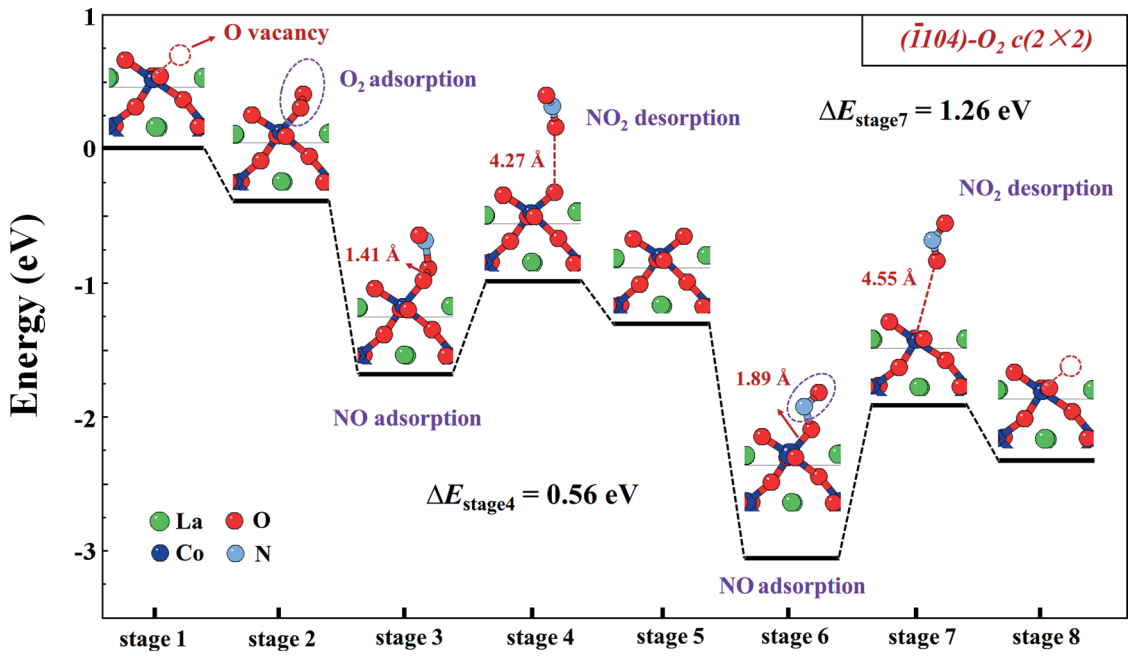

Fig. 5 Energetic scenario of NO oxidation on the $(\bar{1}104)$-O_2 $c(2 \times 2)$ termination, which starts with an O_2 molecule occupying the O vacancy on the surface. The total reaction can be summarized as $2NO + O_2 \rightarrow 2NO_2$, exothermically.

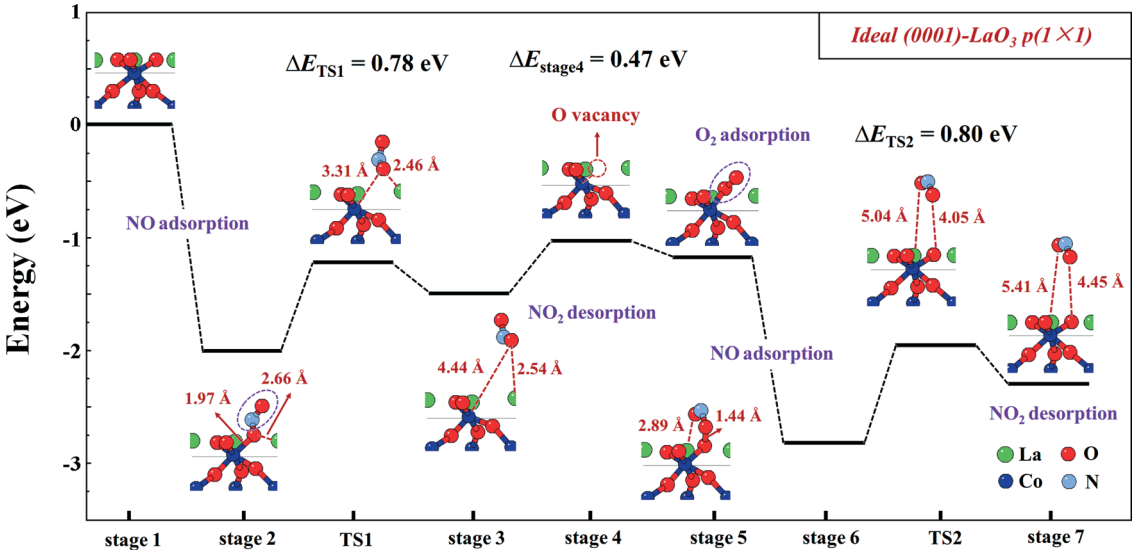

Fig. 6 Energetic scenario of NO oxidation on an ideal (0001)-LaO_3 $p(1 \times 1)$ surface based on the mono-vacancy M–vK mechanism.

trapped by a La atom (stage 3). In the second step, the NO_2 molecule escapes from the La site with an additional barrier of 0.47 eV. This leaves one oxygen vacancy on the surface, and the following step involves a perpendicular adsorption of an O_2 molecule onto the vacancy site. In subsequent steps, the second NO molecule binds to the protruding O atom and forms an adsorbed NO_2 molecule (stage 6 to stage 7) with a desorption barrier of ΔE_{TS2} = 0.80 eV, which is the highest energy barrier along the whole reaction path.

For NO oxidation on (0001)-LaO_3 surfaces with oxygen vacancies, since the reaction with a NO molecule would create an additional oxygen vacancy, the reaction proceeds *via* the Dv M–vK mechanism. Fig. 7 shows the NO oxidation path on the (0001)-LaO_3 $p(1 \times 1)$ surface starting with an oxygen vacancy. As shown in Fig. 7, the NO oxidation path initiates at (2.2) in Scheme 2, as the vacancy is occupied by an NO molecule. The adsorbed NO would bind to an oxygen nearby the vacancy and form NO_2. Similar to the case in Fig. 6, the NO_2 molecule will be trapped by two La atoms and the desorption process is endothermic by 1.18 eV (stage 3 to stage 4). After the desorption of NO_2, a di-vacancy is created on the (0001)-LaO_3 $p(1 \times 1)$ surface. Then, the di-vacancy is occupied by O_2 (stage 5) and the O atoms bind with a Co atom to form a stable structure. The dissociation of the O_2 molecule to fill the di-vacancy shows an activation barrier of 1.54 eV. In the following steps, NO will bind to the ideal surface and react with the lattice oxygen with an energy barrier of 0.78 eV, as shown in Fig. 6. This recovers the (0001)-LaO_3 $p(1 \times 1)$ surface with an oxygen vacancy and completes the NO oxidation cycle. Through the discussion of Fig. 7, the

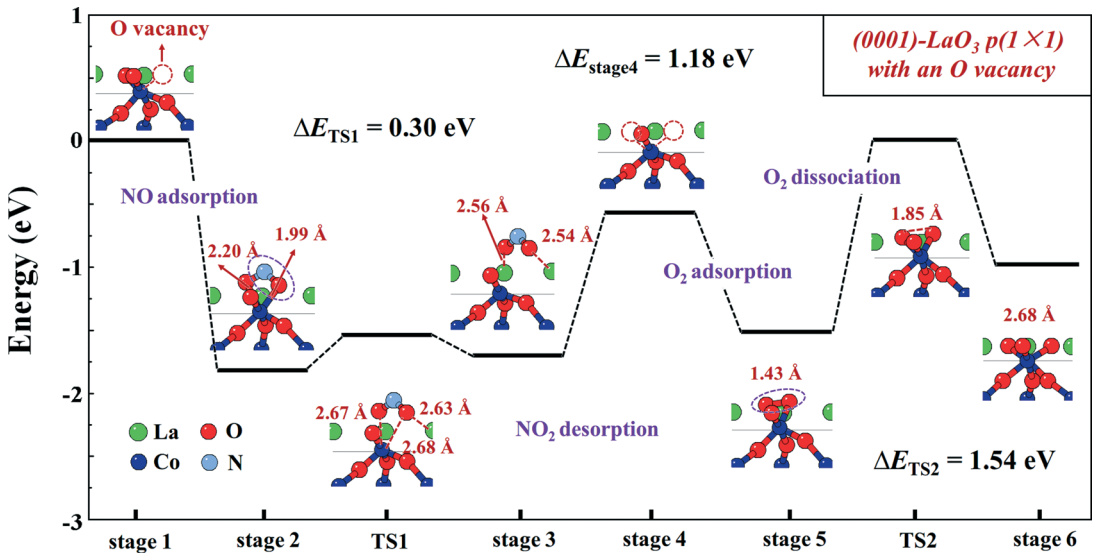

Fig. 7 Energetic scenario of NO oxidation on a (0001)-LaO_3 $p(1 \times 1)$ surface with an oxygen vacancy based on the di-vacancy M–vK mechanism.

RDS step on the (0001)-LaO_3 $p(1 \times 1)$ surface based on the Dv M–vK mechanism is the oxygen dissociation step and this mechanism is less favorable than the Mv M–vK mechanism.

Based on the above discussions, we conclude that the LaO_3 terminated surface has the most promising catalytic activity. The RDSs are NO_2 desorption and O_2 dissociation for the Mv and Dv M–vK mechanisms on (0001)-LaO_3, respectively. However, the Mv M–vK mechanism with the lower RDS barrier (0.80 eV) is preferable over the Dv M–vK mechanism. The best strategy to improve the catalytic performance of $LaCoO_3$ NPs is to maximize the area of LaO_3 terminated surfaces, which can be achieved by tuning the surfactants and controlling the cobalt chemical potentials during the synthesis procedure.

4. Conclusions

We have systematically studied the stability of differently reconstructed $LaCoO_3$ surfaces. From a stability point of view, the $(\bar{1}104)$-O_2 $c(2 \times 2)$, (0001)-LaO_3 $p(1 \times 1)$ and $(1\bar{1}02)$-LaO $p(1 \times 1)$ facets are thermodynamically most stable. The NO oxidation mechanisms on active surfaces have been comprehensively investigated and the (0001)-LaO_3 facet is found to be most active towards NO oxidation. The RDS steps for the Mv– and Dv– M–vK mechanism are NO_2 desorption and O_2 dissociation, respectively. Our results give insight into the reaction mechanism of NO oxidation on hexagonal phase $LaCoO_3$ and could help further optimization of the perovskite catalyst.

Acknowledgements

This work is supported the National Basic Research Program of China (2013CB934800 and 2011CB606401) and National Natural Science Foundation of China (grant 51302094 and 51101064). The authors acknowledge the Thousand Young Talents Plan and Program for Changjiang Scholars and Innovative Research Team in University. The calculations were done at the Texas Advanced Computing Center (TACC) at The University of Texas at Austin (http://www.tacc.utexas.edu).

Notes and references

1 C. H. Bartholomoew and R. J. Farrauto, *Fundamentals of Industrial Catalytic Process*, Wiley, Hoboken, N.J., 2006.
2 M. Tas, R. van Hardeveld and E. M. van Veldhuizen, *Plasma Chem. Plasma Process.*, 1997, **17**, 371–391.
3 B. Hammer, Y. Morikawa and J. K. Nørskov, *Phys. Rev. Lett.*, 1996, **76**, 2141–2144.
4 M. H. Tsai and K. C. Hass, *Phys. Rev. B: Condens. Matter Mater. Phys.*, 1995, **51**, 14616–14625.
5 X. W. Xie, Y. Li, Z. Q. Liu, M. Haruta and W. J. Shen, *Nature*, 2009, **458**, 746–749.
6 L. F. Liotta, H. J. Wu, G. Pantaleo and A. M. Venezia, *Catal. Sci. Technol.*, 2013, **3**, 3085–3102.
7 S. Krishnamoorthy, J. A. Rivas and M. D. Amiridis, *J. Catal.*, 2000, **193**, 264–272.
8 J. Wang, Y. G. Su, X. Q. Wang, J. H. Chen, Z. Zhao and M. Q. Shen, *Catal. Commun.*, 2012, **25**, 106–109.
9 X. J. Yao, F. Gao, Q. Yu, L. Qi, C. J. Tang, L. Dong and Y. Chen, *Catal. Sci. Technol.*, 2013, **3**, 1355.
10 F. Can, S. Berland, S. Royer, X. Courtois and D. Duprez, *ACS Catal.*, 2013, **3**, 1120–1132.
11 H. Li, X. L. Tang, H. H. Yi and L. L. Yu, *J. Rare Earths*, 2010, **28**, 64–68.
12 W. C. Wang, G. McCool, N. Kapur, G. Yuan, B. Shan, M. Nguyen, U. M. Graham, B. H. Davis, G. Jacobs, K. Cho and X. H. Hao, *Science*, 2012, **337**, 832–835.
13 Y. X. Wen, C. B. Zhang, H. He, Y. B. Yu and Y. Teraoka, *Catal. Today*, 2007, **126**, 400–405.
14 C. Zhou, X. Liu, C. Z. Wu, Y. W. Wen, Y. J. Xue, R. Chen, Z. L. Zhang, B. Shan, H. F. Yin and W. G. Wang, *Phys. Chem. Chem. Phys.*, 2014, **16**, 5106–5112.
15 C. H. Kim, G. S. Qi, K. Dahlberg and W. Li, *Science*, 2010, **327**, 1624–1627.
16 S. Khan, R. J. Oldman, F. Corà, C. Catlow, S. French and S. A. Axon, *Phys. Chem. Chem. Phys.*, 2006, **8**, 5207–5222.
17 Z. Z. Chen, C. H. Kim, L. Thompson and W. F. Schneider, *Surf. Sci.*, 2014, **619**, 71–76.
18 P. Ravindran, P. A. Korzhavyi, H. Fjellvåg and A. Kjekshus, *Phys. Rev. B: Condens. Matter Mater. Phys.*, 1999, **60**, 16423–16434.
19 S. Mukhopadhyay, M. W. Finnis and N. M. Harrison, *Phys. Rev. B: Condens. Matter Mater. Phys.*, 2013, **87**, 125132.
20 M. Risch, A. Grimaud, K. J. May, K. A. Stoerzinger, T. J. Chen, A. N. Mansour and Y. Shao-Horn, *J. Phys. Chem. C*, 2013, **117**, 8628–8635.
21 S. M. Zhou, L. F. He, S. Y. Zhao, Y. Q. Guo, J. Y. Zhao and L. Shi, *J. Phys. Chem. C*, 2009, **113**, 13522–13526.
22 S. O. Choi, M. Penninger, C. H. Kim, W. F. Schneider and L. T. Thompson, *ACS Catal.*, 2013, **3**, 2719–2728.
23 Y. L. Lee, J. Kleis, J. Rossmeisl and D. Morgan, *Phys. Rev. B: Condens. Matter Mater. Phys.*, 2009, **80**, 224101.
24 A. Kushima, S. Yip and B. Yildiz, *Phys. Rev. B: Condens. Matter Mater. Phys.*, 2010, **82**, 115435.
25 P. Hohenberg and W. Kohn, *Phys. Rev.*, 1964, **136**, B864–B871.
26 W. Kohn and L. J. Sham, *Phys. Rev.*, 1965, **140**, A1133–A1138.
27 G. Kresse and J. Hafner, *Phys. Rev. B: Condens. Matter Mater. Phys.*, 1993, **47**, 558–561.
28 G. Kresse and J. Hafner, *Phys. Rev. B: Condens. Matter Mater. Phys.*, 1994, **49**, 14251–14269.
29 G. Kresse and J. Hafner, *Comput. Mater. Sci.*, 1996, **6**, 15–50.
30 J. P. Perdew, K. Burke and M. Ernzerhof, *Phys. Rev. Lett.*, 1996, **77**, 3865–3868.
31 G. Kresse and D. Joubert, *Phys. Rev. B: Condens. Matter Mater. Phys.*, 1999, **59**, 1758–1775.
32 H. Y. Kim and G. Henkelman, *J. Phys. Chem. Lett.*, 2012, **3**, 2194–2199.
33 H. Y. Kim and G. Henkelman, *J. Phys. Chem. Lett.*, 2013, **4**, 216–221.
34 V. I. Anisimov, J. Zaanen and O. K. Andersen, *Phys. Rev. B: Condens. Matter Mater. Phys.*, 1991, **44**, 943.
35 A. Rohrbach, J. Hafner and G. Kresse, *Phys. Rev. B: Condens. Matter Mater. Phys.*, 2004, **69**, 075413.

36 A. Rohrbach and J. Hafner, *Phys. Rev. B: Condens. Matter Mater. Phys.*, 2005, **71**, 045405.
37 C. L. Ma and J. Cang, *Solid State Commun.*, 2010, **150**, 1983–1986.
38 F. Aryasetiawan and O. Gunnarsson, *Rep. Prog. Phys.*, 1998, **61**, 237.
39 G. Onida, L. Reining and A. Rubio, *Rev. Mod. Phys.*, 2002, **74**, 601.
40 J. Heyd, G. E. Scuseria and M. Emzerhof, *J. Chem. Phys.*, 2003, **118**, 8207.
41 J. Heyd, G. E. Scuseria and M. Emzerhof, *J. Chem. Phys.*, 2006, **124**, 19906.
42 H. J. Monkhorst and J. D. Pack, *Phys. Rev. B: Solid State*, 1976, **13**, 5188.
43 F. Bottin, F. Finocchi and C. Noguera, *Phys. Rev. B: Condens. Matter Mater. Phys.*, 2003, **68**, 035418.
44 G. H. Chen, Z. F. Hou and X. G. Gong, *Comput. Mater. Sci.*, 2008, **44**, 46–52.
45 C. Herring, *Phys. Rev.*, 1951, **82**, 87.
46 K. Momma and F. Izumi, *J. Appl. Crystallogr.*, 2011, **44**, 1272–1276.
47 G. Henkelman and H. Jónsson, *J. Chem. Phys.*, 2000, **113**, 9978–9985.
48 P. G. Radaelli and S. W. Cheong, *Phys. Rev. B: Condens. Matter Mater. Phys.*, 2002, **66**, 094408.
49 A. Chainani, M. Mathew and D. D. Sarma, *Phys. Rev. B: Condens. Matter Mater. Phys.*, 1992, **46**, 9976–9983.
50 I. A. Nekrasov, S. V. Streltsov, M. A. Korotin and V. I. Anisimov, *Phys. Rev. B: Condens. Matter Mater. Phys.*, 2003, **68**, 235113.
51 J. Kuneš and V. Křápek, *Phys. Rev. Lett.*, 2011, **106**, 256401.
52 S. K. Pandey, A. Kumar, S. Patil, V. R. R. Medicherla, R. S. Singh, K. Maiti, D. Prabhakaran, A. T. Boothroyd and A. V. Pimpale, *Phys. Rev. B: Condens. Matter Mater. Phys.*, 2008, **77**, 045123.
53 H. Y. Wang and W. F. Schneider, *Catal. Today*, 2011, **165**, 49–55.
54 H. Y. Wang, W. F. Schneider and D. Schmidt, *J. Phys. Chem. C*, 2009, **113**, 15266–15273.
55 J. Zhou, G. Chen, K. Wu and Y. H. Cheng, *J. Phys. Chem. C*, 2013, **117**, 12991–12999.
56 C. Noguera, *J. Phys.: Condens. Matter*, 2000, **12**, R367.
57 F. Bechstedt, *Principles of Surface Physics*, Springer-Verlag, New York, 2003.
58 K. Reuter and M. Scheffler, *Appl. Phys. A: Mater. Sci. Process.*, 2004, **78**, 793.
59 S. Piccinin, S. Zafeiratos, C. Stampfl, T. W. Hansen, M. Hävecker, D. Teschner, V. I. Bukhtiyarov, F. Girgsdies, A. Knop-Gericke, R. Schlögl and M. Scheffler, *Phys. Rev. Lett.*, 2010, **104**, 035503.
60 P. Mars and D. W. Van Krevelen, *Chem. Eng. Sci.*, 1954, **3**, 41–59.
61 W. Y. Song and E. J. M. Hensen, *Catal. Sci. Technol.*, 2013, **3**, 3020–3029.
62 H. Y. Kim, H. M. Lee and G. Henkelman, *J. Am. Chem. Soc.*, 2012, **134**, 1560–1570.
63 Z. Say, M. Dogac, E. I. Vovk, Y. E. Kalay, C. H. Kim, W. Li and E. Ozensoy, *Appl. Catal., B*, 2014, **154**, 51–61.

